INTERNATIONAL JOURNAL FOR NUMERICAL METHODS IN FLUIDS
Int. J. Numer. Meth. Fluids 2008; **57**:119–138
Published online 2 October 2007 in Wiley InterScience (www.interscience.wiley.com). DOI: 10.1002/fld.1624

An accurate finite element scheme with moving meshes for computing 3D-axisymmetric interface flows

Sashikumaar Ganesan*,† and Lutz Tobiska

Institute of Analysis and Numerical Computation, Otto-von-Guericke-University, PF4120, D-39016 Magdeburg, Germany

SUMMARY

An accurate finite element scheme for computing 3D-axisymmetric incompressible free surface and interface flows is proposed. It is based on the arbitrary Lagrangian Eulerian (ALE) approach using free surface/interface-resolved moving meshes. Key features like the surface force, consisting of surface tension and the local curvature, and jumps in the density and viscosity over different fluid phases are precisely incorporated in the finite element formulation. The local curvature is approximated by using the Laplace–Beltrami operator technique combined with a boundary approximation by isoparametric finite elements. A new approach is used to derive the 3D-axisymmetric form from the variational form in 3D-Cartesian coordinates. Several test examples show the high accuracy and the robustness of the proposed scheme. Copyright © 2007 John Wiley & Sons, Ltd.

Received 26 March 2007; Revised 23 August 2007; Accepted 24 August 2007

KEY WORDS: free surface flows; interface flows; finite elements; ALE approach; spurious velocities

1. INTRODUCTION

Free surface and interface flows are often encountered in day-to-day life, nature and industrial applications. Computations of these flows have drawn attention of many scientists not only of industrial applications but also of physical interest. Apart from difficulties associated with the numerical computation of fluid flows, the moving free surface/interfaces cause additional problems. In particular, the development of accurate and stable numerical schemes for free surface and interface flows is still a challenging task. An important issue is the precise inclusion of the surface force, which compresses the surface/interface tension and the local curvature on the free

*Correspondence to: Sashikumaar Ganesan, Institute of Analysis and Numerical Computation, Otto-von-Guericke-University, PF4120, 39106 Magdeburg, Germany.
†E-mail: ga.sashikumaar@mathematik.uni-magdeburg.de

Contract/grant sponsor: German Research Foundation; contract/grant number: To143/9

surface/interface. Apart from these difficulties, additional care is needed to handle the jumps in the material properties (density and viscosity) across the interface and to suppress exhibiting spurious velocities (or parasitic currents).

In computations of these flows, either Eulerian or Lagrangian approaches is used. Popular methods in Eulerian approach are the volume-of-fluid (VOF), level-set (LS) and front-tracking (FT) methods. In all these methods, a fixed (or) Eulerian grid is used to solve the Navier–Stokes equations for the fluid flow whereas the free surface/interface capturing/tracking technique differs in each method. In the VOF method [1–4] a colour function, which represents the fractional amount of fluid present in a cell, is used to capture the interface between two phases. The capturing of interface with the LS method [5–8] is simple and relatively easy to implement. In this method a zero LS function is used to capture the interface. The FT method [9, 10] uses a separate one dimension lower moving mesh to track the interface. Each of these methods has its own advantages and disadvantages [11, Chapter 4]. In the Eulerian approach, the inclusion of the surface force and the jumps in the material properties requires additional techniques, such as the continuum surface force (CSF) [12] model and the cutting Heaviside functions. The numerical error caused by these approximation techniques influences the reliability of the computed solution of the problem [13]. Recently, it has been shown in [14] that spurious velocities of a considerable size can occur in case of free surface/interface flows computed on interface non-resolved meshes.

We will use an alternative way, the arbitrary Lagrangian Eulerian (ALE) approach, which avoids the fast mesh distortion known from the pure Lagrangian method. The ALE approach is quite popular in fluid structure interaction problems. For applications to free surface flows in the finite element context, we refer to [15–18]. Since the free surface/interface is resolved by the mesh, the surface force and the different material properties in different phases can be incorporated very accurately in our scheme. We use the Laplace–Beltrami operator technique for approximating the local curvature which avoids the explicit computation of the curvature. Further, a new technique is used to derive the variational form of the 3D-axisymmetric problem. The main idea is to start with the variational form in 3D Cartesian coordinates and to transform the volume as well as the surface integrals into area and line integrals, respectively, by introducing cylindrical coordinates and imposing axisymmetric conditions. In such an approach, the 'artificial' boundary conditions at the symmetry axis appear in a natural way.

The structure of the paper is as follows. First, the governing equations of a typical two-phase flow are given in Section 2. Starting with the variational form in 3D-Cartesian coordinates we derive the 3D-axisymmetric form and discuss the type of boundary conditions appearing at the symmetry axis in a canonical way. In Section 3, all details of the proposed numerical scheme, in particular the discretization in space and time, the ALE approach, the linearization and the elastic mesh update, are discussed. The numerical tests in Section 4 cover the stationary and non-stationary behaviour of a bubble in equilibrium, a freely oscillating droplet, and a rising bubble in a liquid. They demonstrate the high accuracy of the proposed method.

2. MATHEMATICAL MODEL

2.1. Governing equations for two-phase flows

We consider a typical situation of a two-phase flow. Let $\Omega \subset \mathbb{R}^3$ be a cylindrical domain. We assume that Ω contains two immiscible liquids, in particular a liquid droplet $\Omega_1(t)$ completely surrounded

DOI: 10.1002/fld

by another liquid filling the domain $\Omega_2(t)=\Omega\backslash\overline{\Omega}_1(t)$, where $t\in[0,T]$ is the time variable. The interface between the two immiscible liquids is denoted by $\Gamma_F(t):=\partial\Omega_1(t)\cap\partial\Omega_2(t)$. We denote by ρ_k, μ_k the density and dynamic viscosity of the fluid in $\Omega_k(t)$, $k=1,2$.

The fluid flow in Ω is described by the time-dependent incompressible Navier–Stokes equations completed by the initial conditions, the kinematic and force balance at the interface $\Gamma_F(t)$ and boundary conditions at $\partial\Omega$. For simplicity, we consider homogeneous Dirichlet boundary conditions at $\partial\Omega$; however, the approach can be extended to other types of boundary conditions too, see, e.g. [19]. We choose the characteristic values U, L, ρ_1 for velocity, length, density and define the dimensionless density and Reynolds number in different parts of the domain Ω to be

$$\rho(\mathbf{x})=\begin{cases}1 & \text{for } \mathbf{x} \text{ in } \Omega_1(t),\\ \rho_2/\rho_1 & \text{for } \mathbf{x} \text{ in } \Omega_2(t),\end{cases}\qquad Re(\mathbf{x})=\begin{cases}\rho_1 UL/\mu_1 & \text{for } \mathbf{x} \text{ in } \Omega_1(t)\\ \rho_1 UL/\mu_2 & \text{for } \mathbf{x} \text{ in } \Omega_2(t)\end{cases}$$

Then, the Navier–Stokes equations describing the two-phase flow can be expressed in a dimensionless form as

$$\begin{aligned}\rho(\mathbf{x})\left(\frac{\partial\mathbf{u}}{\partial t}+(\mathbf{u}\cdot\nabla)\mathbf{u}\right)-\nabla\cdot(\mathbb{S}_k(\mathbf{u},p))&=\rho(\mathbf{x})\frac{1}{Fr}\mathbf{e} \quad \text{in } \Omega_k(t)\times(0,\mathrm{T}]\\ \nabla\cdot\mathbf{u}&=0 \quad \text{in } \Omega_k(t)\times(0,\mathrm{T}]\\ [\mathbf{u}]=0,\quad \boldsymbol{\tau}_{i,F}[\mathbb{S}(\mathbf{u},p)]\cdot\boldsymbol{\nu}&=0 \quad \text{on } \Gamma_F(t)\times(0,\mathrm{T}]\\ \boldsymbol{\nu}[\mathbb{S}(\mathbf{u},p)]\cdot\boldsymbol{\nu}=-\frac{1}{We}\mathscr{K},\quad \mathbf{u}\cdot\boldsymbol{\nu}&=\mathbf{w}\cdot\boldsymbol{\nu} \quad \text{on } \Gamma_F(t)\times(0,\mathrm{T}]\\ \mathbf{u}&=0 \quad \text{on } \partial\Omega\times(0,\mathrm{T}]\\ \mathbf{u}&=0 \quad \text{on } \Omega_k\times\{0\}\end{aligned}\tag{1}$$

for $k=1,2, i=1,2$, where $\mathbf{u}$ denotes the fluid velocity, $\mathbf{w}$ the interface velocity, p the pressure in the fluid, $\mathscr{K}$ the sum of the principal curvatures, ∇ and $\nabla\cdot$ the gradient and divergence operators, respectively. Further, the notation $[\cdot]$ is used for the jump across the interface, $\mathbf{e}$ for the unit vector opposite to the gravitational force, $\boldsymbol{\nu}$ for the outward unit normal vector with respect to $\Omega_1(t)$ and $\boldsymbol{\tau}_{i,F}, i=1,2$, for tangential vectors on the interface $\Gamma_F(t)$. For a Newtonian incompressible fluid, the dimensionless form of the stress tensor $\mathbb{S}_k(\mathbf{u},p)$ and the velocity deformation tensor $\mathbb{D}(\mathbf{u})$ are given by

$$\mathbb{S}_k(\mathbf{u},p):=\frac{2}{Re(\mathbf{x})}\mathbb{D}(\mathbf{u})-p\mathbb{I},\quad \mathbb{D}(\mathbf{u})=\frac{1}{2}(\nabla\mathbf{u}+\nabla\mathbf{u}^T)\tag{2}$$

where $\mathbb{I}$ is the identity tensor and the superscript T denotes the transpose of the tensor. Finally, the dimensionless Weber and Froude number are given by

$$We=\frac{\rho_1 U^2 L}{\sigma},\quad Fr=\frac{U^2}{Lg}$$

with the gravitational constant g and the surface tension coefficient σ.

DOI: 10.1002/fld

Remark 1
When choosing the characteristic velocity as $U=\sqrt{Lg}$, the Weber number becomes the so-called Eötvös number

$$Eo=\frac{\rho_1 g L^2}{\sigma}$$

and the Froude number reduces to 1.

2.2. Variational formulation

Starting point of a finite element discretization is a weak formulation of (1). To this end let $V:=(H_0^1(\Omega))^3$ and $Q:=L_0^2(\Omega)$ be the usual Sobolev spaces. We multiply the momentum and mass balance equations of (1) by test functions $\mathbf{v}\in V$ and $q\in Q$, respectively, integrate over Ω, and use the integration by parts in each subdomain $\Omega_k(t)$. After incorporating the boundary conditions, the variational form of (1) reads as given below:

For given $\Omega(0)$ and $\mathbf{u}(0,\mathbf{x})$, find $(\mathbf{u}, p)\in V\times Q$ such that

$$\left(\rho(x)\frac{\partial \mathbf{u}}{\partial t},\mathbf{v}\right)+a(\mathbf{u},\mathbf{u},\mathbf{v})-b(p,\mathbf{v})+b(q,\mathbf{u})=(f,\mathbf{v})\quad \forall(\mathbf{v},q)\in V\times Q \tag{3}$$

Here, $(\cdot,\cdot)$ denotes the inner product in $L^2(\Omega)$ and its vector-valued versions and

$$a(\hat{\mathbf{u}},\mathbf{u},\mathbf{v})=2\int_\Omega \frac{1}{Re(\mathbf{x})}\mathbb{D}(\mathbf{u}):\mathbb{D}(\mathbf{v})\,\mathrm{d}\mathbf{x}+\int_\Omega \rho(x)(\hat{\mathbf{u}}\cdot\nabla)\mathbf{u}\cdot\mathbf{v}\,\mathrm{d}\mathbf{x}$$

$$b(q,\mathbf{v})=\int_\Omega q\ \nabla\cdot\mathbf{v}\,\mathrm{d}\mathbf{x}$$

$$(f,\mathbf{v})=\frac{1}{Fr}\int_\Omega \rho(x)\mathbf{e}\cdot\mathbf{v}\,\mathrm{d}\mathbf{x}-\frac{1}{We}\int_{\Gamma_F(t)}\mathscr{K}\mathbf{v}\cdot\mathbf{v}\,\mathrm{d}\gamma_F$$

To evaluate the above interface integral, we first replace the curvature term by the Laplace–Beltrami operator, then use the integration by parts formula on the surface $\Gamma_F(t)$ to obtain

$$\frac{1}{We}\int_{\Gamma_F(t)}\mathscr{K}\mathbf{v}\cdot\mathbf{v}\,\mathrm{d}\gamma_F=\frac{1}{We}\int_{\Gamma_F(t)}\underline{\Delta} id_{\Gamma_F}\cdot\mathbf{v}\,\mathrm{d}\gamma_F=-\frac{1}{We}\int_{\Gamma_F(t)}\underline{\nabla} id_{\Gamma_F}:\underline{\nabla}\mathbf{v}\,\mathrm{d}\gamma_F$$

Here, the restriction $id_{\Gamma_F(t)}:\Gamma_F(t)\to\Gamma_F(t)$ denotes the identity mapping on $\Gamma_F(t)$. Since we consider only closed interfaces, no additional integrals over the boundary of the interface appear, see [11] for a more general case.

Remark 2
In case that a fluid in $\Omega_1(t)$ is surrounded by air, the air flow in $\Omega_2(t)$ is often neglected and replaced by the assumption of a constant pressure field ($\rho_2\ll 1$). Thus, $\mathbf{u}(t)=\mathbf{0}$, $p=\text{const}$ in $\Omega_2(t)$ and the integrals over Ω in (3) reduce to integrals over $\Omega_1(t)$. We end up with a free surface flow problem by considering the fluid phase in $\Omega_1(t)$ only.

DOI: 10.1002/fld

2.3. 3D-axisymmetric variational formulation

In contrast to the standard approach of starting with the differential equations in cylindrical coordinates and looking for a suitable variational formulation, we will derive the 3D-axisymmetric weak form in the 2D-meridian domain Φ of Ω directly from the weak form (3) in 3D-Cartesian coordinates. For this, we transform the volume and surface integrals in 3D into area and line integrals in 2D by introducing cylindrical coordinates and imposing irrotational, axisymmetric conditions. In such a way the space-dimension of the problem is reduced by one. This approach leads naturally to boundary conditions along the 'artificial rotational axis' which are already partly included in the weak form.

Let us define the Cartesian coordinates in terms of cylindrical polar coordinates r (the radial coordinate), ϕ (the azimuthal coordinate) and z (the axial coordinate) by

$$x = r\cos\phi, \quad y = r\sin\phi, \quad z = z$$

where r is the radial distance from the origin, and ϕ is the counter-clockwise angle from the x-axis. In terms of x and y, we have

$$r(x,y) = \sqrt{x^2+y^2}, \quad \phi(x,y) = \arctan(y/x), \quad 0 \leqslant \phi(x,y) < 2\pi$$

Let $\mathbf{u} = (u_1, u_2, u_3)$ be the velocity vector in Cartesian coordinates and $\mathbf{u}_c = (u_r, u_\phi, u_z)$ be the velocity vector in cylindrical coordinates. We define the Cartesian velocity components in terms of the cylindrical velocity components by

$$u_1 = u_r\cos\phi - u_\phi\sin\phi, \quad u_2 = u_r\sin\phi + u_\phi\cos\phi, \quad u_3 = u_z$$

Now, we use the fact that the cylindrical velocity components u_r, u_ϕ, u_z and the pressure $\tilde{p} = \tilde{p}(r,\phi,z)$ are independent of ϕ, and $u_\phi = 0$. Hence, we have

$$\begin{aligned} u_1(x,y,z) &= u_r(r(x,y),z)\cos\phi(x,y), \quad u_2(x,y,z) = u_r(r(x,y),z)\sin\phi(x,y) \\ u_3(x,y,z) &= u_z(r(x,y),z), \quad p(x,y,z) = \tilde{p}(r(x,y),z) \end{aligned} \tag{4}$$

Similarly, for the test functions $\mathbf{v} = (v_1, v_2, v_3)$ and q we have

$$\begin{aligned} v_1(x,y,z) &= v_r(r(x,y),z)\cos\phi(x,y), \quad v_2(x,y,z) = v_r(r(x,y),z)\sin\phi(x,y) \\ v_3(x,y,z) &= v_z(r(x,y),z), \quad q(x,y,z) = \tilde{q}(r(x,y),z) \end{aligned} \tag{5}$$

To illustrate our approach, let us consider the bilinear forms

$$(\rho\mathbf{u}, \mathbf{v}) = \int\int\int_\Omega \rho(x,y,z)\mathbf{u}\cdot\mathbf{v}\,\mathrm{d}x\,\mathrm{d}y\,\mathrm{d}z \tag{6}$$

$$(p, \nabla\cdot\mathbf{v}) = \int\int\int_\Omega p\ \nabla\cdot\mathbf{v}\,\mathrm{d}x\,\mathrm{d}y\,\mathrm{d}z \tag{7}$$

with $\Omega \subset \mathbb{R}^3$ and transform them into the axisymmetric bilinear forms. Consider first the integral (6), which arises from the discretization of the time derivative in (3). Using (4) and (5) we obtain the

DOI: 10.1002/fld

3D-axisymmetric form of (6) as

$$\int\int\int_\Omega \rho(x,y,z)\,\mathbf{u}\cdot\mathbf{v}\,\mathrm{d}x\,\mathrm{d}y\,\mathrm{d}z = \int_0^{2\pi}\int\int_\Phi \rho\,(u_r v_r\cos^2\phi + u_r v_r \sin^2\phi + u_z v_z) r\,\mathrm{d}r\,\mathrm{d}z\,\mathrm{d}\phi$$
$$= 2\pi\int\int_\Phi \rho\,(u_r v_r + u_z v_z) r\,\mathrm{d}r\,\mathrm{d}z$$

where Φ is the meridian of Ω. Next, integral (7) becomes

$$\int\int\int_\Omega p\ \nabla\cdot\mathbf{v}\,\mathrm{d}x\,\mathrm{d}y\,\mathrm{d}z = \int_0^{2\pi}\int\int_\Phi \left[\tilde{p}\left(\frac{\partial v_r}{\partial r}+\frac{1}{r}v_r+\frac{\partial v_z}{\partial z}\right)\right] r\,\mathrm{d}r\,\mathrm{d}z\,\mathrm{d}\phi$$
$$= 2\pi\int\int_\Phi \left[\tilde{p}\left(\frac{\partial v_r}{\partial r}+\frac{1}{r}v_r+\frac{\partial v_z}{\partial z}\right)\right] r\,\mathrm{d}r\,\mathrm{d}z$$

Similarly, the 3D-axisymmetric form of the deformation tensor and convective integrals becomes

$$\int\int\int_\Omega \frac{1}{Re(x,y,z)}\mathbb{D}(\mathbf{u}):\mathbb{D}(\mathbf{v})\,\mathrm{d}x\,\mathrm{d}y\,\mathrm{d}z$$
$$= 2\pi\int\int_\Phi \frac{1}{Re}\left[\frac{\partial u_r}{\partial r}\frac{\partial v_r}{\partial r}+\frac{u_r v_r}{r^2}+\frac{1}{2}\left(\frac{\partial u_r}{\partial z}+\frac{\partial u_z}{\partial r}\right)\left(\frac{\partial v_r}{\partial z}+\frac{\partial v_z}{\partial r}\right)+\frac{\partial u_z}{\partial z}\frac{\partial v_z}{\partial z}\right] r\,\mathrm{d}r\,\mathrm{d}z$$
$$\int\int\int_\Omega \rho\,(\hat{\mathbf{u}}\cdot\nabla\mathbf{u})\cdot\mathbf{v}\,\mathrm{d}x\,\mathrm{d}y\,\mathrm{d}z$$
$$= 2\pi\int\int_\Phi \rho\left[\left(\hat{u}_r\frac{\partial u_r}{\partial r}+\hat{u}_z\frac{\partial u_r}{\partial z}\right)v_r+\left(\hat{u}_r\frac{\partial u_z}{\partial r}+\hat{u}_z\frac{\partial u_z}{\partial z}\right)v_z\right] r\,\mathrm{d}r\,\mathrm{d}z$$

The surface integral over $\Gamma_F(t)$ can be transformed into a line integral over the surface generating curve $L\subset\partial\Phi$ as follows:

$$\frac{1}{We}\int_{\Gamma_F(t)}\underline{\nabla} id_{\Gamma_F}:\underline{\nabla}\mathbf{v}\,\mathrm{d}\gamma_F = \frac{2\pi}{We}\int_L\left(\frac{\partial id_r}{\partial l}\frac{\partial v_r}{\partial l}+\frac{id_r v_r}{r^2}+\frac{\partial id_z}{\partial l}\frac{\partial v_z}{\partial l}\right) r\,\mathrm{d}l$$

where $\partial/\partial l$ denotes the tangential derivative and $id=(id_r,id_z)=(r,z)$ is the identity.

Note that the integrals of the transformed linear, bilinear and trilinear form, respectively, are well defined provided that

$$p,q\in L^2_r(\Phi):=\left\{w:\int_\Phi r w^2\,\mathrm{d}r\,\mathrm{d}z<\infty\right\},\quad u_r,v_r\in H^1_r(\Phi):=\left\{w:w,\frac{\partial w}{\partial r},\frac{\partial w}{\partial z}\in L^2_r(\Phi)\right\}$$

and, additionally, $r^{-1/2}u_r, r^{-1/2}v_r\in L^2(\Phi)$. The last requirement leads to the boundary condition $u_r=0$ along the symmetry axis $r=0$. The boundary part of $\partial\Phi$ along $r=0$ can be considered as an artificial boundary since it is not a boundary of $\partial\Omega$. We mention that along $r=0$ there is another boundary condition 'hidden', which becomes visible when assuming regularity and integrating by

DOI: 10.1002/fld

parts to generate the strong formulation of the underlying system of differential equations. This 'hidden' boundary condition can be written as

$$\left.\frac{\partial u_z}{\partial r}\right|_{r=0} = 0 \tag{8}$$

The Dirichlet-type boundary condition $u_r = v_r = 0$ on $r = 0$ is taken into account by imposing it into ansatz and test spaces. This leads to different spaces for the two component (u_r, u_z) of the velocity. For more details on existence and uniqueness (for small data) in weighted Sobolev spaces, we refer to [20, 21]. It should be mentioned that the 3D-axisymmetric form is—modulo some additional terms—similar to the 2D plane formulation. This offers the possibility to extent 2D finite element codes for 3D-axisymmetric problems quite easily.

3. NUMERICAL SCHEME

3.1. ALE approach

In our case the subdomains $\Omega_1(t)$ and $\Omega_2(t)$ representing the two phases are time dependent but not $\Omega = \Omega_1(t) \cup \Gamma_F(t) \cup \Omega_2(t)$. In order to simplify the notation in the following, we write $\Omega(t)$ instead of Ω having in mind that Ω decomposes into time-dependent subdomains. As we mentioned in the Introduction, we use the ALE approach to track moving boundaries and interfaces. To rewrite the weak form (3) in the ALE form, we define a family of mappings $\mathscr{A}_t$, which at each time $t \in [0, \mathrm{T})$ map a point (the ALE coordinate) $\mathbf{Y} \in \hat{\Omega}$ of the reference domain $\hat{\Omega}$ onto a point (the Eulerian coordinate) $\mathbf{X}$ of the current domain $\Omega(t)$, i.e.

$$\mathscr{A}_t : \hat{\Omega} \to \Omega(t), \quad \mathscr{A}_t(\mathbf{Y}) = \mathbf{X}(\mathbf{Y}, t)$$

We assume that the mapping $\mathscr{A}_t$ is homeomorphic, i.e. $\mathscr{A}_t \in C^0(\overline{\hat{\Omega}})$ is invertible with continuous inverse $\mathscr{A}_t^{-1} \in C^0(\overline{\Omega(t)})$. Further, we assume that the mapping

$$t \to \mathbf{X}(\mathbf{Y}, t), \quad \mathbf{Y} \in \hat{\Omega}$$

is differentiable almost everywhere in $[0, T)$. The vector function $\mathbf{u}$ in (3) is defined on the Eulerian frame. Now, we define $\hat{\mathbf{u}} : \hat{\Omega} \times (0, \mathrm{T}) \to \mathbb{R}^3$ by

$$\hat{\mathbf{u}}(\mathbf{Y}, t) = \mathbf{u}(\mathscr{A}_t(\mathbf{Y}), t) \quad \forall \mathbf{Y} \in \hat{\Omega}$$

which is the corresponding function on the ALE frame. Further, the time derivative of $\mathbf{u}$ on the ALE frame is defined by

$$\left.\frac{\partial \mathbf{u}}{\partial t}\right|_{\hat{\Omega}} (\mathbf{X}, t) = \frac{\partial \hat{\mathbf{u}}}{\partial t}(\mathscr{A}_t^{-1}(\mathbf{X}), t)$$

Here, the notation $|_{\hat{\Omega}}$ is used to indicate that the time derivative is taken on the ALE frame. Then, the term

$$\mathbf{w}(\mathbf{X}, t) = \left.\frac{\partial \mathbf{X}}{\partial t}\right|_{\hat{\Omega}}$$

DOI: 10.1002/fld

represents the domain velocity. Now, applying the chain rule with respect to the time derivative on $\mathbf{u}\circ\mathscr{A}_t$ on the ALE frame, we obtain

$$\left.\frac{\partial \mathbf{u}}{\partial t}\right|_{\hat{\Omega}} = \left.\frac{\partial \mathbf{u}}{\partial t}\right|_{\mathbf{X}} + \left.\frac{\partial \mathbf{X}}{\partial t}\right|_{\hat{\Omega}} \cdot \nabla_{\mathbf{X}}\mathbf{u} = \left.\frac{\partial \mathbf{u}}{\partial t}\right|_{\mathbf{X}} + \mathbf{w}\cdot\nabla_{\mathbf{X}}\mathbf{u} \tag{9}$$

where $\nabla_{\mathbf{X}}$ denotes the gradient with respect to the Eulerian coordinate and the time derivative on the Eulerian frame is denoted by $|_{\mathbf{X}}$. Using (9) in (3), we obtain

$$\left(\rho(x)\left.\frac{\partial \mathbf{u}}{\partial t}\right|_{\hat{\Omega}}, \mathbf{v}\right) + a(\mathbf{u}-\mathbf{w};\mathbf{u},\mathbf{v}) - b(p,\mathbf{v}) + b(q,\mathbf{u}) = (f,\mathbf{v}) \tag{10}$$

which is the ALE form of Equation (3). Formulation (10) implies the Eulerian form and the Lagrangian form for choosing $\mathbf{w}=\mathbf{0}$ and $\mathbf{w}=\mathbf{u}$, respectively. From a theoretical point of view, the choice of the reference domain is arbitrary, and often the initial domain $\Omega(0)$ is taken as the reference domain. However, in case of large deformations of the domain $\Omega(t)$, it is better to choose a domain $\Omega(t^*)\approx\Omega(t)$ with $t^*<t$ as the reference domain to preserve the mesh quality. In our computations, we always use $\Omega(t_n)$ as the reference domain in the ALE approach, i.e. the domain of the previous time step $t^*=t_n$.

3.2. Discretization and linearization

We use the second-order, strongly A-stable fractional-step-ϑ scheme [22, 23] as a time discretization. Further, the non-linear convection term is linearized by a fixed point iteration. Starting with the solution of the previous time step $\mathbf{u}^0 := \mathbf{u}^{\text{old}}$, we iterate $\mathbf{u}^k \longmapsto \mathbf{u}^{k+1}$ based on

$$\int_{\Omega(t)} (\mathbf{u}^{\text{new}}\cdot\nabla)\mathbf{u}^{\text{new}}\mathbf{v}\,\mathrm{d}\mathbf{x} \approx \int_{\Omega(t)} (\mathbf{u}^{k}\cdot\nabla)\mathbf{u}^{k+1}\mathbf{v}\,\mathrm{d}\mathbf{x} \tag{11}$$

until the residual measured in the Euclidean norm is below a given threshold or the given maximal number of iterations is reached. Then, we set $\mathbf{u}^{\text{new}} := \mathbf{u}^{k_{\text{stop}}}$.

As in [24], we use a semi-implicit discretization of the curvature term

$$-\frac{1}{We}\int_{\Gamma_F(t_{n+1})} \underline{\nabla} id_{\Gamma_F(t_{n+1})} : \underline{\nabla}\mathbf{v}\,\mathrm{d}\gamma_F \approx -\frac{1}{We}\int_{\Gamma_F(t_n)} \underline{\nabla}(id_{\Gamma_F(t_n)} + \delta t_n \mathbf{u}^{n+1}) : \underline{\nabla}\mathbf{v}\,\mathrm{d}\gamma_F$$

with the time step $\delta t_n = t_{n+1} - t_n$. Thus, the curvature term is splitted into an explicit term on the right-hand side of the equation

$$-\frac{1}{We}\int_{\Gamma_F(t_n)} \underline{\nabla} id_{\Gamma_F(t_n)} : \underline{\nabla}\mathbf{v}\,\mathrm{d}\gamma_F$$

and an implicit term on the left-hand side of the equation

$$+\frac{\delta t_n}{We}\int_{\Gamma_F(t_n)} \underline{\nabla}\mathbf{u}^{n+1} : \underline{\nabla}\mathbf{v}\,\mathrm{d}\gamma_F$$

Note that this term on the left-hand side is symmetric and positive semi-definite and—compared with a fully explicit approach—adds stability to the system.

Since in the ALE approach the computed velocities are used to move the free surface and interface, high accuracy is required. Moreover, mass conservation should be guaranteed and spurious

DOI: 10.1002/fld

velocities—if there are some—should be suppressed. Our focus is on second-order inf–sup stable finite element approximations avoiding spurious pressure oscillations [25]. A popular inf–sup stable second-order element is the Taylor–Hood element, consisting of continuous, piecewise quadratic and continuous, piecewise linear functions on triangles (P_2/P_1) or continuous, piecewise biquadratic and continuous, piecewise bilinear functions on quadrilateral (Q_2/Q_1). Unfortunately, for this type of finite elements the pressure is approximated by continuous functions, which generate spurious velocities in the neighbourhood of the interface [14]. For suppressing spurious velocities one would be more interested to use discontinuous, piecewise linear functions for the pressure approximation combined with continuous, piecewise quadratic approximations for the velocity components (P_2/P_1^{disc}). However, this finite element pair is not inf–sup stable on a general regular family of meshes [26, 27]. Indeed, in [28] (2D case) and recently in [29] (3D case), the inf–sup stability has been shown only for a restricted class of macro-element-type meshes satisfying certain properties. It seems to be very difficult to maintain these properties on a sequence of moving meshes. Therefore, we enrich the velocity space by adding cubic bubble functions to combine the properties of suppressing spurious velocities (discontinuous pressure approximations) and inf–sup stability on a general shape regular family of meshes [30]. We denote this element pair shortly by $P_2^{\text{bubble}}/P_1^{\text{disc}}$. Alternatively, on quadrilaterals we can use continuous, piecewise biquadratic functions to approximate the velocity components and discontinuous, piecewise linear functions for the pressure, i.e. Q_2/P_1^{disc} [25, 31]. Note that the reason for a better mass conservation of discontinuous, piecewise polynomial pressure approximations is the elementwise vanishing of the first integral moments of the divergence of the velocity field.

3.3. Mesh generation and mesh moving technique

The domain is triangulated by an interface/boundary-resolved triangular mesh using the mesh generator 'triangle' [32]. We also use decompositions of the domain into quadrilaterals starting with a coarse mesh which is successively refined by connecting the midpoints of opposite sides.

Our mesh moving technique consists of two steps. First, we advect the free surface/interface points with the computed flow velocity, and then displace the inner points in an elastic solid manner according to the displacement of the free surface/interface points.

We advect the free surface/interface points $\mathbf{X}^n$ solving

$$\frac{\mathrm{d}\mathbf{X}}{\mathrm{d}t} = \mathbf{u}(\mathbf{X}, t)$$

with the implicit Euler scheme

$$\mathbf{X}^{n+1} = \mathbf{X}^n + (t_{n+1} - t_n)\mathbf{u}^{n+1}$$

to obtain the new position of the free surface/interface points. Then, we compute from the free surface/interface displacement $\mathbf{d}^n = \mathbf{X}^{n+1} - \mathbf{X}^n$ the displacement Ψ^n of the inner points by solving the linear elasticity problems:

$$\nabla \cdot \mathbb{T}(\Psi^n) = 0 \ \text{ in } \Omega_k(t_n), \quad \Psi^n(\mathbf{x}^n) = \mathbf{d}^n \ \text{ on } \partial\Omega_k(t_n), \ \ k = 1, 2$$

where $\mathbb{T}$ denotes the stress tensor given by

$$\mathbb{T}(\phi) = \lambda_1(\nabla \cdot \phi)\mathbb{I} + 2\lambda_2 \mathbb{D}(\phi)$$

DOI: 10.1002/fld

The problem is discretized by continuous, piecewise linear finite elements on the same mesh, which is used for the flow computation. Here, λ_1 and λ_2 are the Lame constants, chosen to be $\lambda_1 = \lambda_2 = 1$ in our numerical tests. Further, the mesh velocity becomes

$$\mathbf{w}^n = \Psi^n / (t_{n+1} - t_n)$$

By using the ALE approach with this elastic mesh update we avoided a quick distortion of the mesh. Further, neither re-meshing nor interpolation is needed at every time step. However, occasionally the distortion of the mesh becomes very large and at that time the re-meshing is unavoidable. Thus, we implemented an automatic re-meshing procedure in the code MooNMD [33] which will be called automatically if the mesh quality criterion is not fulfilled. While re-meshing, we generate first a new mesh by using the old free surface/interface points and then interpolate the solutions from the old to the newly generated mesh.

3.4. Solution of the saddle point problem

For solving saddle point problems fast geometric multi-grid methods on fixed grids are available in the code MooNMD [17, 33, 34]. These iterative solvers are based on a hierarchy of mesh levels, which is quite expensive (especially due to re-meshing) to generate on a sequence of moving meshes. Therefore, we solved the linearized system directly using the direct solver 'UMFPACK' [35–38].

4. NUMERICAL RESULTS

We consider different test examples to demonstrate the accuracy of the proposed numerical scheme. First, we study a 3D-axisymmetric bubble in equilibrium under zero gravity condition. In this case, no flow field is generated, i.e. $\mathbf{u} = \mathbf{0}$ and the pressure is piecewise constant in the domains $\Omega_k(t) = \Omega_k$ for $t \geqslant 0$ and has a jump across the interface $\Gamma_F(t) = \Gamma_F$. We solve this stationary Stokes problem with given interface Γ_F numerically with different finite element discretizations to obtain an impression on the size of spurious velocities. Next, we relax the assumption of a given fixed interface, consider the problem as time-dependent and determine the dynamics of the interface by numerically solving the time-dependent Navier–Stokes equation. A reliable method should again not generate a flow field and simulate a bubble in equilibrium. The kinetic energy caused by spurious velocities and the mass fluctuation will be studied numerically over time for different finite element discretizations. As a second test case, we consider a 3D-axisymmetric freely oscillating droplet and compare the computational results with analytical approximations and fully 3D computations. Finally, the computation of a rising 3D-axisymmetric bubble problem will show that the proposed method is also applicable for large density jumps.

4.1. Static bubble for a given interface

We consider a 3D-axisymmetric bubble in equilibrium under zero gravity condition. In this case, the stationary Stokes problem without the kinematic boundary condition

$$\mathbf{u} \cdot \mathbf{v} = \mathbf{w} \cdot \mathbf{v} \quad \text{on } \Gamma_F$$

is solved. We expect that no flow field will be generated, in particular, that the velocity at the interface will be zero. Let $[0, 2] \times [0, 4]$ be the meridian domain Φ and the half circle of radius 1

DOI: 10.1002/fld

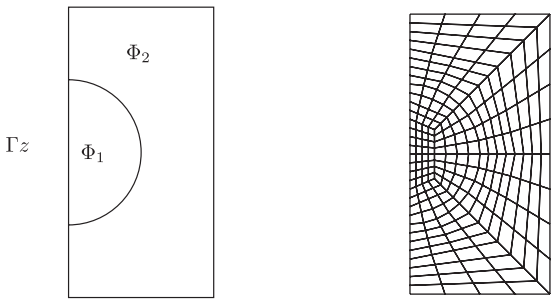

Figure 1. The meridian domain $\Phi = \Phi_1 \cup \Phi_2$ (left) of the 3D-axisymmetric static bubble problem and its triangulation (right) at level 0. Γz denotes the artificial boundary on the rotational axis.

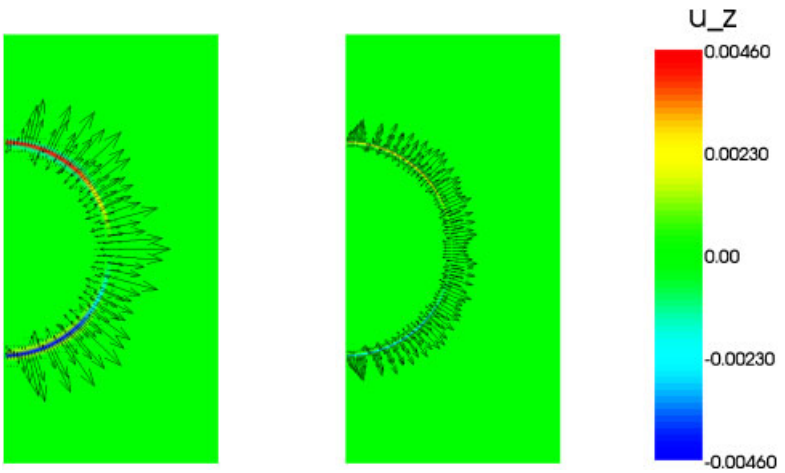

Figure 2. Spurious velocities generated in the axisymmetric static bubble problem with Q_2/Q_1 discretization at refinement level 2 (left) and 3 (right).

with centre at $(0, 1)$ represents the bubble. We triangulate the meridian domain Φ using interface-resolved quadrilateral meshes. The computational grid is obtained by successively refining an initial coarse grid, see Figure 1 (right) for the grid level 0. For studying the influence of continuous *versus* discontinuous pressure approximations, two different inf–sup stable discretizations, namely Q_2/Q_1 and Q_2/P_1^{disc}, have been used. The dynamic viscosities and the surface tension have been set to be $\mu_1 = \mu_2 = 1\,\text{N s/m}^2$ and $\sigma = 1\,\text{N/m}$, respectively. For the continuous pressure approximation Q_1, the generated spurious velocities are visualized in Figure 2 on the refinement levels 2 and 3. The arrows indicate the direction and the magnitude of the spurious velocities at the corresponding points. The colours correspond to the magnitude of the axial velocity component u_z. We clearly see that the magnitude of spurious velocities becomes smaller when the mesh is refined. In the case of the discountinuous pressure approximation P_1^{disc}, the spurious velocities are much smaller and would be not visible in the same scale. Indeed, the velocity error $||\mathbf{u} - \mathbf{u}_h|| = ||\mathbf{u}_h||$ (since $\mathbf{u} = \mathbf{0}$) measured in L_2-norm and H^1-semi norm is about three order of magnitude smaller for

DOI: 10.1002/fld

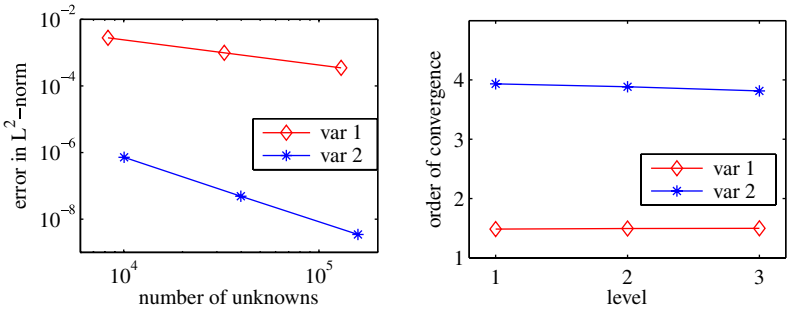

Figure 3. Velocity error in L^2-norm (left) and order of convergence (right) for the static bubble problem. Var 1: Q_2/Q_1 and Var 2: Q_2/P_1^{disc}.

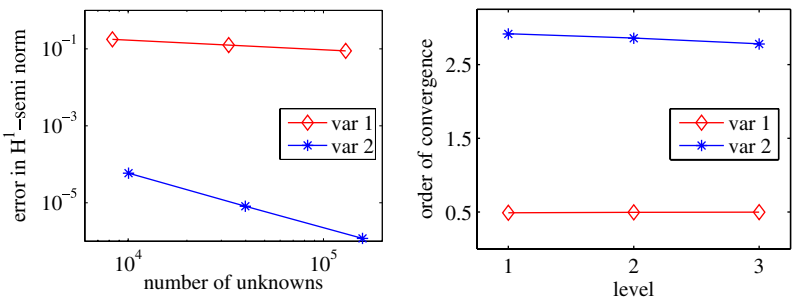

Figure 4. Velocity error in H^1-semi norm (left) and order of convergence (right) for the static bubble problem. Var 1: Q_2/Q_1 and Var 2: Q_2/P_1^{disc}.

the discontinuous pressure approximation than for the continuous ones. Figures 3 and 4 show, in addition, the rates of convergence order for the two discretizations.

4.2. Static bubble for an unknown interface

In contrast to the previous section we now consider the time-dependent case and apply the kinematic boundary condition. We start with the same initial configuration and expect no movement of the bubble since it is in equilibrium. However, due to the presence of spurious velocities the interface will be moved by the ALE technique. The time-dependent Navier–Stokes equations are solved by the $P_2^{\text{bubble}}/P_1^{\text{disc}}$ discretization on triangular interface-resolved meshes. Iso-parametric elements and the Laplace–Beltrami technique have been used to achieve optimal convergence rates [14].

In this test case, we used the densities $\rho_1 = 1.23\,\text{kg/m}^3$, $\rho_2 = 1000\,\text{kg/m}^3$, the dynamic viscosities $\mu_1 = 1.73 \times 10^{-5}\,\text{N s/m}^2$, $\mu_2 = 1 \times 10^{-3}\,\text{N s/m}^2$, and the surface tension $\sigma = 0.073\,\text{N/m}$. The chosen characteristic length of $L = d_0 = 2 \times 10^{-3}\,\text{m}$ and the characteristic velocity $U = 0.14\,\text{m/s}$ result in the Weber number $We = 0.537$ and the Reynolds number $Re = 280$ with respect to the outer phase. The computations have been performed on two different meshes: a coarse grid with a minimal and maximal diameter of the triangular cells of $h_{\min} = 0.0157$ and $h_{\max} = 0.158$, and a fine grid

DOI: 10.1002/fld

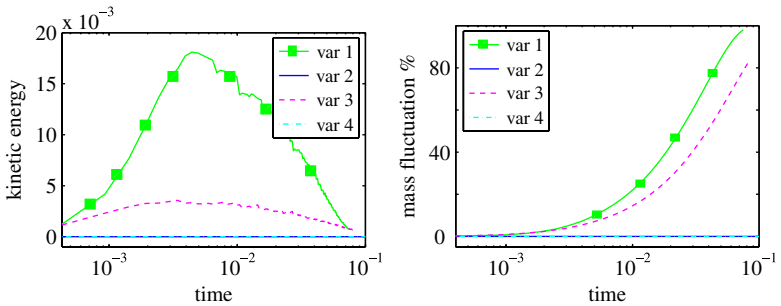

Figure 5. Kinetic energy (left) and mass fluctuation (right) over time in the static bubble problem due to spurious velocities. Var 1: P_2/P_1 on coarse grid, Var 2: P_2/P_1^{disc} on coarse grid, Var 3: P_2/P_1 on fine grid and Var 4: P_2/P_1^{disc} on fine grid.

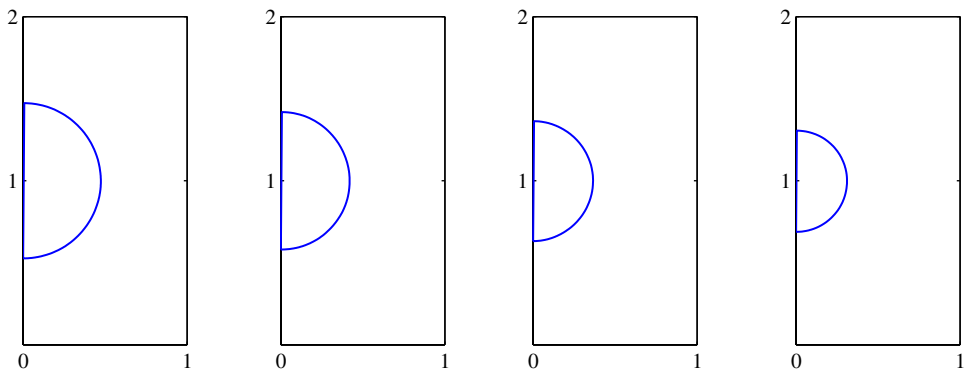

Figure 6. Shrinking of the bubble for the P_2/P_1 discretization on the fine mesh. Bubble shapes at dimensionless times $t=0.01$, 0.03, 0.06, 0.07 (from left to right).

with $h_{\min}=0.00785$ and $h_{\max}=0.0969$. The effect of spurious velocities can be demonstrated by calculating the (dimensionless) kinetic energy of the bubble

$$E=\int_{\Phi_1} r\mathbf{u}(t)\cdot\mathbf{u}(t)\,\mathrm{d}r\,\mathrm{d}z \tag{12}$$

Another important quantity for evaluating the accuracy of a numerical scheme is the mass fluctuation factor

$$M_F(t)=\frac{|\Omega_1(0)-\Omega_1(t)|}{|\Omega_1(0)|}\times 100\% \tag{13}$$

where $|\Omega_1(t)|$ denotes the volume of the bubble $\Omega_1(t)$ at time t.

The kinetic energy (due to the spurious velocities) and the mass fluctuation in this test case are plotted in Figure 5. In variant 1 (P_2/P_1, coarse mesh) the dimensionless kinetic energy increases to a maximal value of about 17×10^{-3} and reduces to zero eventually when the mass of the bubble reduces to zero. This effect is less visible in variant 3 (P_2/P_1, fine mesh). An interesting observation

DOI: 10.1002/fld

in this computation is that spurious velocities are almost suppressed in the discontinuous pressure approximation. Indeed, the magnitudes of spurious velocities are numerically zero over a large time interval which is not the case for continuous pressure approximations. Further, as noticed at the end of Section 3.2, the discontinuous pressure approximation shows a better mass conservation, see Figure 5 (right). However, for the continuous pressure approximation, the mass loss in the bubble is quite large and the bubble starts to shrink in variants 1 and 3, see Figure 6.

4.3. Freely oscillating droplet

In this section we present numerical results for a freely oscillating 3D-axisymmetric droplet. The fluid is assumed to be in rest at time $t=0$ in a zero gravity environment. At the beginning, the shape of the bubble will be different from its equilibrium shape and will converge to the equilibrium for $t\to\infty$. This is an example of a surface tension driven one-phase flow (cf. Remark 2 in Section 2.2).

4.3.1. Comparison with a fully 3D simulation. In [15], fully 3D simulations for a droplet of the initial shape

$$x^2+y^2+(z/a)^2=1, \quad a=1.2$$

has been performed for $Re=300$ and $We=1$. We consider the same problem but in an axisymmetric formulation. The trajectory of the top tip point on the z-axis computed by the 3D-axisymmetric simulation is plotted in Figure 7 (left) and is in good agreement with the trajectory obtained in [15]. The mass fluctuation in our simulation for a grid with $h_{\min}=0.02$, $h_{\max}=0.11$, and 15 562 degrees of freedom is plotted in Figure 7 (right). After 6 periods the mass fluctuation is about 0.014% for 15 562 degrees of freedom, which is an excellent value showing the accuracy of the numerical scheme. The flow field in the droplet during oscillations is visualized in Figure 8. The colours in each image of Figure 8 represent the magnitude of the pressure field in the droplet, where blue and red indicate minimal and maximal values, respectively.

Further, we compare the frequency ω_{num} after n period, and the damping factor δ given as

$$\omega_{\text{num}}:=\frac{n}{t_n} \quad \text{and} \quad \delta:=\sqrt[n]{\frac{\mathscr{T}_{r_{\max}}(t_n)-r(t_\infty)}{\mathscr{T}_{r_{\max}}(t_0)-r(t_\infty)}}$$

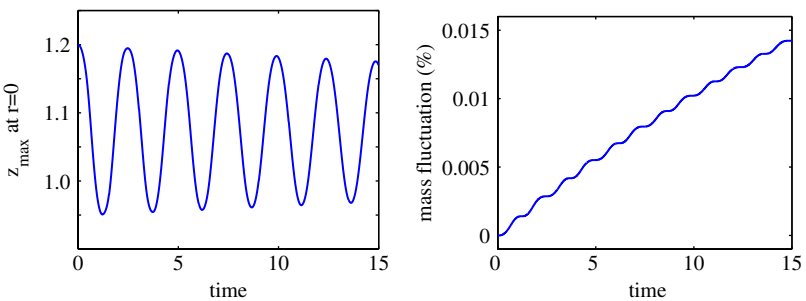

Figure 7. Trajectory of the top tip on the z-axis (left) and mass fluctuation (right) in a freely oscillating droplet computation with $Re=300$, $We=1$.

DOI: 10.1002/fld

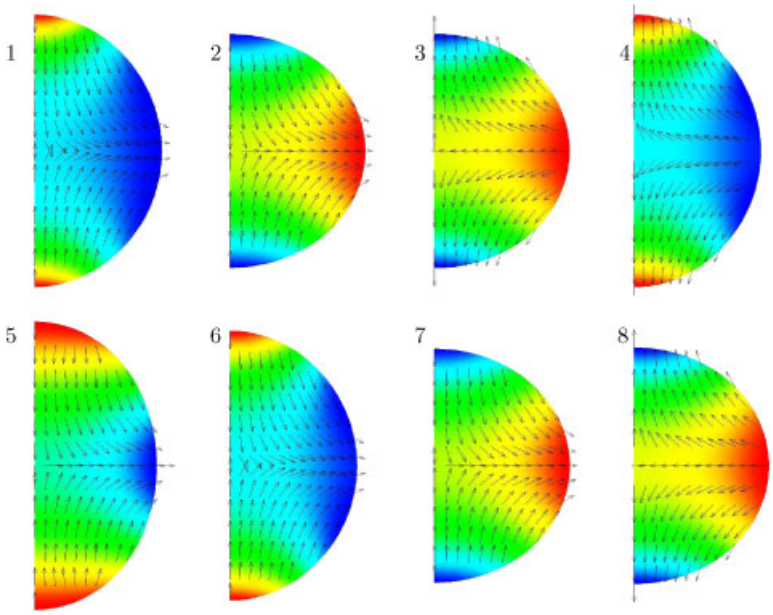

Figure 8. A sequence of shapes and flow fields at different instances of a freely oscillating droplet, dimensionless timings from image 1 are $t=0.5, 1.0, 1.5, 2.0, 2.5, 3.0, 3.5, 4.0$. Colours represent the magnitude of the pressure field in the droplet.

with the values computed in [15]. Here, t_n is the time at the nth period, $\mathscr{T}_{r_{\max}}(t)$ is the trajectory of the tip which has its largest radius at time $t=t_0$ and $r(t_\infty)$ is the radius of the spherical droplet with the same volume as the initial droplet. The frequency and the damping factor obtained in our computation are $\omega_{\text{num}}=0.403$ and $\delta=0.966$. Although a rather coarse 2D mesh has been used to calculate these values, the results are in good agreement with the values 0.406 and 0.966, respectively, obtained in [15] by a fully 3D simulation at refinement level 12.

4.3.2. Comparisons with analytical approximations. The oscillating frequency ω_{the} of a freely oscillating inviscid, incompressible droplet can be approximated by a linear stability analysis. For the 3D case and for small initial perturbations of the equilibrium given by

$$r(\phi)=r_0(1+\varepsilon S_k(\phi)), \quad \varepsilon \ll 1$$

the following formula for the frequency has been obtained in [39, 40]:

$$\omega_{\text{the}}^2=\frac{k(k-1)(k+2)\sigma}{\rho r_0} \tag{14}$$

Here, R is the distance from the centre of the droplet to the free surface, k denotes the order of the spherical harmonic $S_k(\phi)$, ρ is the density, σ the surface tension, and ε is a small positive constant. Furthermore, it is mentioned in [40] that a water droplet of initial radius less than the critical value $R_c=2.3\times10^{-8}$ m is *damped aperiodically*. To compare our numerical results with these theoretical predictions, we consider a water droplet with three different radii: (i) $r_0=2.3\times10^{-9}$ m,

DOI: 10.1002/fld

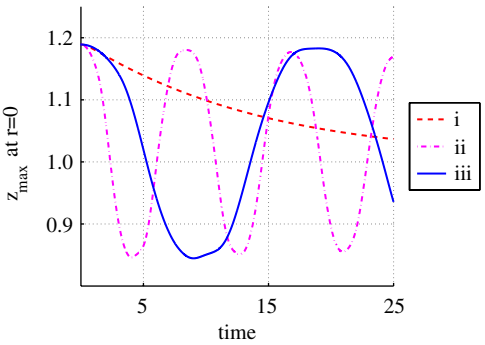

Figure 9. Trajectories of the top tip on the z-axis in three variants of a freely oscillating droplet over the dimensionless time.

Table I. Comparisons of theoretical and numerical frequencies, and damping factor in three variants for a freely oscillating droplet.

Variant	ω_{the}	ω_{num}	δ	$M_{F_{\max}}$
(ii)	121.1434	119.0527	0.9663	0.005
(iii)	10.8353	10.5129	0.9653	0.001

which is less than the critical value, (ii) $r_0 = 1 \times 10^{-3}$ m, (iii) $r_0 = 5 \times 10^{-3}$ m. The used material parameters of the water droplet are the surface tension $\sigma = 0.074\,\text{N/m}$, the density $\rho = 1000\,\text{kg/m}^3$ and the dynamic viscosity $\mu = 0.001\,\text{N s/m}^2$. These parameters together with $L = r_0$ lead to the set of dimensionless parameters:

(i) $Re = 2.3$, $We = 31$ (where $U = 10^3\,\text{m/s}$),
(ii) $Re = 1000$, $We = 13.5$ (where $U = 1\,\text{m/s}$),
(iii) $Re = 5000$, $We = 67.5$ (where $U = 1\,\text{m/s}$).

Computations are made for these three cases, the mode $k = 2$ and $\varepsilon = 0.3$. The trajectories of the top tip point are shown in Figure 9. As predicted in the theoretical analysis [40], for the variant (i) the droplet *damped aperiodically* in our computations, see Figure 9. Furthermore, the oscillating frequency is much higher in variant (ii) compared with variant (iii). The numerically computed frequencies for the variants (ii) and (iii) are compared with the theoretical frequencies predicted by linear stability analysis, see Table I. This table also shows the damping factors and the mass fluctuation.

4.4. Rising bubble

For illustrating the robustness of the proposed numerical scheme we compute a rising air bubble in water where large jumps in the material properties have to be handled. In the computations, Ω_1 and Ω_2 denote the air and water region, respectively. The following material parameters have been used; the densities $\rho_1 = 1.23\,\text{kg/m}^3$, $\rho_2 = 1000\,\text{kg/m}^3$, the dynamic viscosities $\mu_1 = 1.73 \times 10^{-5}\,\text{N s/m}^2$, $\mu_2 = 1 \times 10^{-3}\,\text{N s/m}^2$, the surface tension $\sigma = 0.073\,\text{N/m}$, and the gravitational constant $g = 9.8\,\text{m/s}^2$. We assume that at time $t = 0$, the bubble is of spherical shape with diameter

DOI: 10.1002/fld

$d_0 = 2.5 \times 10^{-3}$ m and is in rest. The diameter and the height of the cylindrical vessel containing the bubble are 5×10^{-3} and 1×10^{-1} m, respectively. We use the characteristic values $L = 2d_0$ and $U = \sqrt{Lg}$, which result in the dimensionless numbers $Re = 1107$ and $Eo = 3.36$ with respect to the outer phase. After scaling the space variables we obtain the computational meridian domain $\Phi_1 = (0,\ 0.5) \times (0\ 2)$, which contains Φ_2 of dimensionless radius $r_0 = 0.25$ and centre $(0,\ 0.5)$.

In our computation, we calculate a few quantities such as the sphericity, the rise velocity, and the z component of the centre of mass. The sphericity of the bubble is defined by

$$S_{\Omega_1}(t) = \frac{A_e}{A} = \frac{\text{surface area of volume-equivalent sphere}}{\text{surface area of the bubble}}$$

This implies that for a spherical bubble we obtain $S_{\Omega_1}(t) = 1$ and for any deformed bubble we obtain $S_{\Omega_2}(t) < 1$. In the 3D-axisymmetric configuration, the surface area of a volume-equivalent sphere and the surface area of the bubble are calculated by

$$A_e = 4\pi \left(\frac{3}{4\pi} \int\int_{\Phi_1} r \, dr \, dz \right)^{2/3}, \quad A = 2\pi \int_L r \, dl$$

where $L \subset \partial\Phi_1$ denotes the bubble surface generating curve. The rise velocity (u_z component) of the bubble can be calculated by

$$U_{\text{rise}} = \frac{2\pi U}{|\Omega_1|} \int\int_{\Phi_1} u_z r \, dr \, dz$$

where $|\Omega_1|$ denotes the volume of the bubble. If the rise velocity reaches for $t \to \infty$ a stationary value, then this value is called a *terminal velocity*. The z component of the centre of mass is

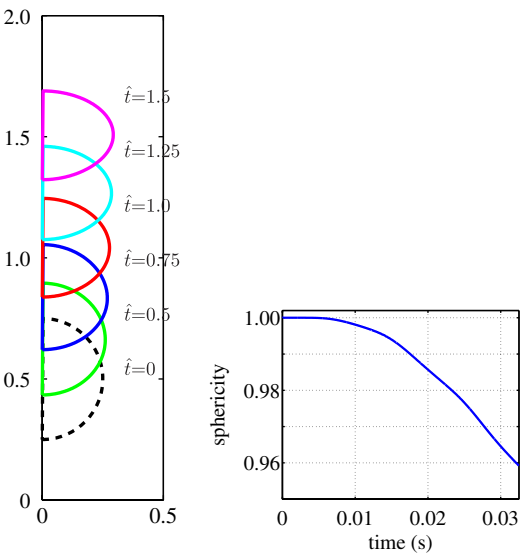

Figure 10. Shape (left) and the sphericity (right) of the bubble at different times.

DOI: 10.1002/fld

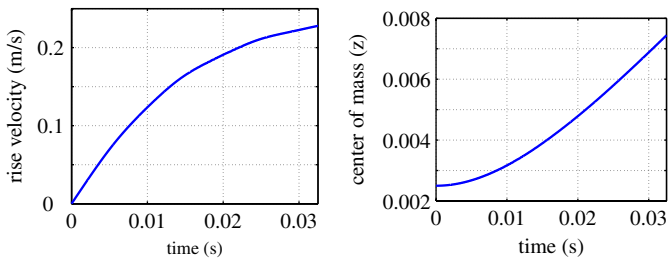

Figure 11. Rise velocity (left) and centre of mass (right) of the bubble over time.

computed using

$$Z_c = \frac{2\pi L}{|\Omega_1|} \int\int_{\Phi_1} zr \, dr \, dz$$

The computed shapes and the sphericity of the bubble are shown in Figure 10. It can clearly be seen that the spherical bubble changes its form to an elliptic shape during the transition. Further, the computed rise velocities and the positions of the centre of mass are shown in Figure 11. After 1 s, the rise velocity reaches a stationary value.

For the considered set of data, it has been observed in experiments (see Figure 7.3 in [41]) that the shape of the bubble belongs to the ellipsoidal regime. Further, the terminal velocity of 3×10^{-1} m (approximately) has been reported. The computed shape and the terminal velocity are in good agreement with these experimental observations.

5. CONCLUDING REMARKS

A finite element scheme for computing free surface and interface flows has been presented in this paper. The highlights of the numerical algorithm are the 3D-axisymmetric derivation from the variational form, the Laplace–Beltrami operator technique for curvature approximation, the ALE approach with moving meshes to track the free surface/interface and capable of computing almost spurious velocity free solutions. Even on problems with large jumps in material parameters the proposed numerical scheme works well without loss of accuracy.

An array of numerical computations is made for a static and freely oscillating 3D-axisymmetric droplet using this numerical scheme. The computed quantities are both qualitatively and quantitatively in good agreement with fully 3D simulations and with analytical approximations. The robustness with respect to jumps in the material parameter is visible in the rising bubble test problem. These studies demonstrate the validity and the accuracy of the proposed numerical scheme.

ACKNOWLEDGEMENT

This work has been partially supported by the German Research Foundation (DFG) through the grant To143/9.

DOI: 10.1002/fld

REFERENCES

1. Hirt CW, Nichols BD. Volume of fluid (VOF) method for the dynamics of free boundaries. *Journal of Computational Physics* 1981; **39**:201–225.
2. Rider WJ, Kothe DB. Reconstructing volume tracking. *Journal of Computational Physics* 1998; **141**:112–152.
3. Pilliod JE, Puckett EG. Second-order accurate volume-of-fluid algorithms for tracking material interfaces. *Journal of Computational Physics* 2004; **199**(2):465–502.
4. Annaland MVS, Deen NG, Kuipers JAM. Numerical simulation of gas bubbles behaviour using a three-dimensional volume of fluid method. *Chemical Engineering Science* 2005; **60**(11):2999–3011.
5. Osher S, Sethian JA. Fronts propagating with curvature dependent speed: algorithms based on Hamilton–Jacobi formulations. *Journal of Computational Physics* 1988; **79**:12–49.
6. Sussman M, Smereka P, Osher S. A level set approach for computing solutions to incompressible two-phase flow. *Journal of Computational Physics* 1994; **114**(1):146–159.
7. Sussman M, Puckett EG. A coupled level set and volume-of-fluid method for computing 3d axisymmetric incompressible two-phase flows. *Journal of Computational Physics* 2000; **162**:301–337.
8. Gross S, Reichelt V, Reusken A. A finite element based level set method for two-phase incompressible flows. *Computing and Visualization in Science* 2006; **9**(4):239–257.
9. Unverdi SO, Tryggvason G. A front-tracking method for viscous, incompressible multi-fluid flows. *Journal of Computational Physics* 1992; **100**:25–37.
10. Tryggvason G, Bunner B, Esmaeeli A, Juric D, Al-Rawahi N, Tauber W, Han J, Nas S, Jan YJ. A front-tracking method for the computations of multiphase flow. *Journal of Computational Physics* 2001; **169**:708–759.
11. Ganesan S. Finite element methods on moving meshes for free surface and interface flows. *Ph.D. Thesis*, Otto-von-Guericke-Universität, Fakultät für Mathematik, Magdeburg, 2006.
12. Brackbill JU, Kothe DB, Zemach C. A continuum method for modeling surface tension. *Journal of Computational Physics* 1992; **100**:335–354.
13. Tornberg AK. Interface tracking methods with application to multiphase flows. *Ph.D. Thesis*, Royal Institute of Technology, Stockholm, 2000.
14. Ganesan S, Matthies G, Tobiska L. On spurious velocities in incompressible flow problems with interfaces. *Computer Methods in Applied Mechanics and Engineering* 2007; **196**:1193–1202.
15. Bänsch E. Finite element discretization of the Navier–Stokes equations with a free capillary surface. *Numerische Mathematik* 2001; **88**:203–235.
16. Nobile F. Numerical approximation of fluid-structure interaction problems with application to haemodynamics. *Ph.D. Thesis*, École Polytechnique Fédérale de Lausanne, 2001.
17. Matthies G. Finite element methods for free boundary value problems with capillary surfaces. *Ph.D. Thesis*, Otto-von-Guericke-Universität, Fakultät für Mathematik, Magdeburg, 2002.
18. Nithiarasu P. An arbitrary Lagrangian–Eulerian (ALE) formulation for free surface flows using the characteristic-based split (CBS) scheme. *International Journal for Numerical Methods in Fluids* 2005; **12**:1415–1428.
19. Ganesan G, Tobiska L. Computations of flows with interfaces using arbitrary Lagrangian–Eulerian method. *Proceedings of ECCOMAS CFD*, Egmond aan Zee, The Netherlands, 2006.
20. Bernardi C, Dauge M, Maday Y. *Spectral Methods for Axisymmetric Domains*. Elsevier: Paris, 1999.
21. Ruas V. Mixed finite element methods with discontinuous pressures for axisymmetric stokes problem. *Zeitschrift fur Angewandte Mathematik und Mechanik* 2003; **83**(4):249–264.
22. Rannacher R. Incompressible viscous flows. In *Encyclopedia of Computational Mechanics*, vol. 3, Chapter 6, Stein E, de Borst R, Hughes TJR (eds). Wiley: New York, 2004; 155–182.
23. Turek S. *Efficient Solvers for Incompressible Flow Problems. An Algorithmic and Computational Approach*. Springer: Berlin, 1999.
24. Bänsch E. *Numerical Methods for the Instationary Navier–Stokes Equations with a Free Capillary Surface*. Habilitationsschrift, Albert-Ludwigs Universität, 2001.
25. Girault V, Raviart PA. *Finite Element Methods for Navier–Stokes Equations*. Springer: Berlin, Heidelberg, New York, 1986.
26. Scott LR, Vogelius M. Conforming finite element methods for incompressible and nearly incompressible continua. In *Large-scale Computations in Fluid Mechanics*, *Part 2* (*La Jolla, Calif., 1983*), Lectures in Applied Mathematics, vol. 22. American Mathematical Society: Providence, RI, 1985; 221–244.
27. Scott LR, Vogelius M. Norm estimates for a maximal right inverse of the divergence operator in spaces of piecewise polynomials. *RAIRO*, *Modélisation Mathématique at Analyse Numérique* 1985; **19**:111–143.

DOI: 10.1002/fld

28. Qin J. On the convergence of some low order mixed finite elements for incompressible fluids. *Ph.D. Thesis*, Pennsylvania State University, 1994.
29. Zhang S. A new family of stable mixed finite elements for the 3D Stokes equations. *Mathematics of Computation* 2005; **74**(250):543–554.
30. Crouzeix M, Raviart PA. Conforming and nonconforming finite element methods for solving the stationary stokes equations I. *RAIRO*, *Analyse Numérique* 1973; **7**:33–76.
31. Matthies G, Tobiska L. The inf–sup condition for the mapped $Q_k/P_{k-1}^{\mathrm{disc}}$ element in arbitrary space dimensions. *Computing* 2002; **69**(2):119–139.
32. Shewchuk JR. Triangle: engineering a 2D quality mesh generator and delaunay triangulator. In *Applied Computational Geometry*: *Towards Geometric Engineering*, Lin MC, Manocha D (eds). Lecture Notes in Computer Science, vol. 1148. Springer: Berlin, May 1996; 203–222. *From the First ACM Workshop on Applied Computational Geometry*.
33. John V, Matthies G. MooNMD—a program package based on mapped finite element methods. *Computing and Visualization in Science* 2004; **6**(2–3):163–170.
34. John V, Knobloch P, Matthies G, Tobiska L. Non-nested multi-level solvers for finite element discretizations of mixed problems. *Computing* 2002; **68**:313–341.
35. Davis TA. Algorithm 832: UMFPACK V4.3—an unsymmetric-pattern multifrontal method. *ACM Transactions on Mathematical Software* 2004; **30**(2):196–199.
36. Davis TA. A column pre-ordering strategy for the unsymmetric-pattern multifrontal method. *ACM Transactions on Mathematical Software* 2004; **30**(2):167–195.
37. Davis TA, Duff IS. A combined unifrontal/multifrontal method for unsymmetric sparse matrices. *ACM Transactions on Mathematical Software* 1999; **25**(1):1–20.
38. Davis TA, Duff IS. An unsymmetric-pattern multifrontal method for sparse *LU* factorization. *SIAM Journal on Matrix Analysis and Applications* 1997; **18**(1):140–158.
39. Chandrasekhar S. *Hydrodynamics and Hydromagnetic Stability*. Clarendon Press: Oxford, 1961.
40. Lamb H. *Hydrodynamics*. Cambridge University Press: Cambridge, 1932.
41. Clift R, Grace JR, Weber ME. *Bubbles*, *Drops and Particles*. Academic Press: New York, 1978.

DOI: 10.1002/fld